Front. Struct. Civ. Eng. 2022, 16(5): 600–614
https://doi.org/10.1007/s11709-022-0821-5

RESEARCH ARTICLE

Effect of cavity defect on the triaxial mechanical properties of high-performance concrete

Yanbin ZHANG, Zhe WANG*, Mingyu FENG

School of Civil Engineering, Beijing Jiaotong University, Beijing100044, China
**Corresponding author. E-mail: zhwang@bjtu.edu.cn*

ABSTRACT The stress concentration of pipe structure or cavity defect has a great effect on the mechanical properties of the high-performance concrete (HPC) members in deep underground locations. However, the behaviour of HPC with cavities under triaxial compression is not understood, especially when pressurized liquid flows into the fractures from the cavity. This study aims to investigate the effect of the cavity and the confining pressure on the failure mechanisms, strengths, and deformation properties of HPC with a new experimental scheme. In this experiment, the pressurized liquid can only contact the surface of the sample in the cavity, while the other surfaces are isolated from the pressurized liquid. To further explore the effect of the cavity, the same experiments are also conducted on sealed and unsealed intact samples without a cavity. The failure modes and stress-strain curves of all types of the samples are presented. Under various confining pressures, all the samples with a cavity suffer shear failure, and there are always secondary tensile fractures initiating from the cavity sidewall. Additionally, it can be determined from the failure modes and the stress-strain curves that the shear fractures result from the sidewall failure. Based on the different effects of the cavity on the lateral deformations in different directions, the initiation of the sidewall fracture is well predicted. The experimental results show that both the increase of the confining pressure and the decrease of the cavity size are conducive to the initiation of sidewall fracture. Moreover, the cavity weakens the strength of the sample, and this study gives a modified Power-law criterion in which the cavity size is added as an impact factor to predict the strength of the sample.

KEYWORDS high-performance concrete, cavity, conventional triaxial compression, pressurized liquid, modified power-law criterion

1 Introduction

Due to the high strength, self-consolidating workability, durability, and ductility, high-performance concrete (HPC) has been widely used in dams, offshore oil production platforms, and some other engineering applications. In some concrete members in a state of three-dimensional compression, pipes are necessary, such as diversion cavity and sand discharge cavity at the bottom of dams. Additionally, cavities exist as a common type of defect in concrete. Under triaxial compression, the stress concentration of the provision of such cavities can result in the initiation of the failure, and then the pressurized liquid flows into the fractures through the cavity leading to loss of strength, stiffness, or stability. It is very important to know the effect of the cavities on the mechanical properties of HPC under triaxial compression.

Previous experimental studies on the mechanical properties of concrete with cavities were usually carried out under uniaxial compression [1–5]. The results showed that the provision of the cavity could weaken the strength and ductility of the concrete. Research on the effect of cavities on the mechanical properties of HPC under uniaxial compression is rare. But research on the mechanical properties of the intact HPC samples under triaxial compression has been plentiful [6–13]; many failure criteria have been presented to predict the effect of the confining pressure on the strength of HPC. However, experimental research on the effect of cavities on the triaxial mechanical properties of HPC has not been found in existing literature.

The effect of the cavities on triaxial mechanical

Article history: Received Nov 3, 2021; Accepted Jan 2, 2022

properties have been studied for rocks in existing literature [14–26], and three types of fractures have been found to originate around a cavity: primary fracture, remote fracture, and sidewall fracture (often called compressive fracture, spalling, and slabbing, respectively, in some literature) [23–28]. The primary fractures originate from the tensile stress concentration area. The remote fractures begin under combined tension and compression. The sidewall fractures originate from the compressive stress concentration area. However, not all of these three types of fractures can occur in various compression conditions. The cavity size has a great effect on the failure mode of the sample under triaxial compression. When the confining pressure is large and the cavity size is small, only the sidewall fractures usually originate from the cavity [15,16]. The sidewall fracture is the most complex of the three types of fractures because of its starting points in the region of high stress gradient and pure compression.

Zhou et al. [29,30] presented a phase field model for simulating quasi-static and dynamic fracture in rock, and the phase field model was proven to model the fracture initiation, propagation coalescence, and branching in rock. In addition, the modified phase field model has been used to model compressive-shear fracture [31]. However, the failure mechanisms around the cavity in HPC under triaxial compression are not clear. The material properties and mechanical characteristics of rock and concrete are quite different, so research on the triaxial mechanical properties of HPC with cavities is urgently needed.

As a new type of HPC, reactive powder concrete (RPC) has the properties of homogeneous, high-strength, and low permeability [32]. A reduction in the size of coarse aggregates and a decrease in the water-to-cement ratio contribute to reducing the permeability of RPC, and the addition of silica fume also helps decrease the porosity as its particles fill empty spaces between the aggregates and cement paste [33–35]. Tam et al. [36] and Roux et al. [37] reported that the permeability coefficient of RPC was typically lower than that of normal strength concrete by one or two orders of magnitude. Li and Huang [38] have stated that the RPC is impermeable. The low-permeability of RPC reduces the interference factors in the research. Therefore, RPC becomes an ideal material for studying the influence of the pressurized liquid on the failure mechanism of HPC.

This article provides an experimental method for researchers studying rock-like materials, and provides reliable mechanical properties of HPC with a cavity to help designers and structural code workers.

2 Materials and experimental procedures

2.1 Sample preparation

RPC is a new type of HPC with many good mechanical properties [32]. Based on the low-permeability [33–35], RPC was chosen to study the triaxial mechanical properties of HPC with a cavity, and all the samples were made of the same mortar mixture. The materials used for the samples were as follows: 1) ordinary Portland cement P.O.52.5R (an average diameter of 14.5 μm, a density of 3120 kg/m^3, and a specific surface area of 3850 m^2/kg); 2) silica fume (a diameter of 0.1–0.3 μm, a density of 2214 kg/m^3, and a specific surface area of 23310 m^2/kg); 3) quartz sand (a diameter of 0.16–0.63 mm and a stacking density of 1750 kg/m^3) as fine aggregates; 4) quartz powder (an average diameter of 10 μm and a stacking density of 240 kg/m^3); 5) 3301 MH polycarboxylate superplasticizer as a water reducer; 6) defoamer to reduce air bubbles in the mortar; 7) tap water. The material proportions are given in Table 1. All the samples were of the same size: 175 mm × 70.7 mm × 41 mm. For the samples with a cavity, there was a circular cavity in the center of the sample (Fig. 1(a)). The cavity were in four different diameters: 2, 5, 7, and 10 mm. Corresponding to the diameter of the cavity, the samples are referred to as SPH2, SPH5, SPH7, and SPH10, respectively. To distinguish the samples with a cavity from the intact samples without a cavity, the samples with a cavity are referred to as SPH. In addition, the sealed intact samples without a cavity are referred to as SPI, and the unsealed intact samples without a cavity are referred to as UPI (Table 2).

The production process of the sample was divided into the following steps. Firstly, a smooth iron bar 41mm long was fixed in the center of the steel mold (but this procedure was omitted for UPI and SPI). The iron bars came in four different diameters, namely, 2, 5, 7, and 10 mm. Secondly, the mortar was stirred evenly and then was poured into the steel molds. Thirdly, the poured molds were placed into a standard curing room and demolded 24 h later. Fourthly, the iron bar was removed. Fifthly, to speed up the reaction of the materials, the demolded samples were cured in a steam curing box with a temperature of 90 °C for 120 h. Finally, the samples were stored in the standard curing room again, and all the

Table 1 Mix proportions of the samples

cement material		quartz powder	quartz sand	admixture		
cement	silica fume			water	water reducer	defoamer
1	0.18	0.27	1	0.2	0.018	0.001

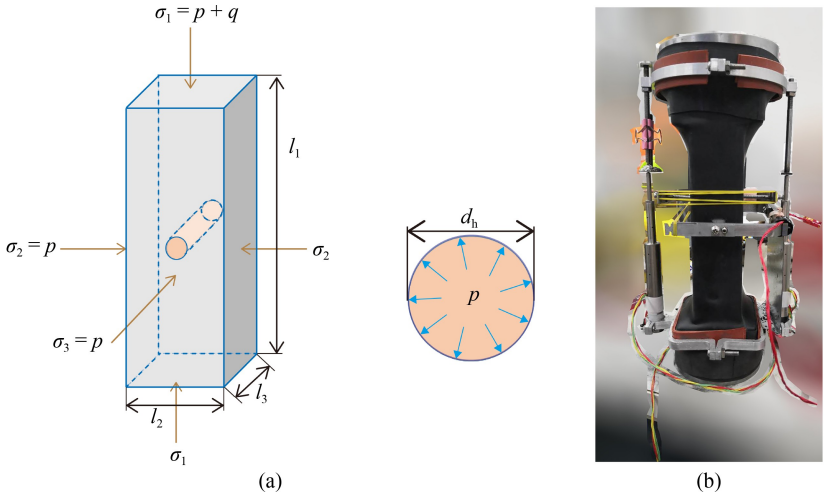

Fig. 1 The assembly of the sample and the force diagram: (a) force diagram of the sample; (b) assembly of the sample. Note: l_1 = 175 mm, l_2 = 70.7 mm, l_3 = 41 mm; q is the axial load; p is the confining pressure; the cavity axis is parallel to l_3.

Table 2 Types of the sample

d_h (mm)	sample	sealing condition
0	SPI	all the surfaces fully sealed
0	UPI	all the surfaces not sealed
2	SPH2	the pressurized liquid could flow into the cavity, while the other surfaces of the sample were sealed
5	SPH5	
7	SPH7	
10	SPH10	

Note: d_h is the diameter of the cavity.

samples were tested within one month after they were removed from the steam curing box.

2.2 Testing methods

Before assembling the sample, three pieces of PTFE 0.1 mm thick were placed between the sample and the indenter, and some lithium-based lubricant was added between the PTFE films to fully reduce the friction. For SPH, some hot melt adhesive was smeared on four sides of the surfaces of the sample, and then a layer of heat-shrinkable tube was used to cover the sample before the hot melt adhesive solidified. Attention was paid to preventing bubbles from forming during the shrinkage of the heat-shrinkable tube. After the hot melt adhesive solidified, the heat-shrinkable tube and the sample could be firmly bonded together, so that the sample was isolated from contacting the pressurized oil. Additionally, a pinhole was left in the heat-shrinkable tube at the cavity to allow the pressurized oil to flow in, and some dense fiber was placed in the cavity to prevent the crushed concrete from flowing into the oil outside the heat-shrinkable tube. The extensometer for measuring the lateral strain (ε_2) of the wide side (l_2) was placed at the same height as the cavity, while the extensometer for measuring the lateral strain (ε_3) of the narrow side (l_3) was placed within 5 mm above the cavity (ε_1, ε_2, and ε_3 were the strains corresponding to l_1, l_2, and l_3, see Fig. 1(a)). Two LVDT sensors were fixed symmetrically to the lateral side of the indenters to measure the axial strain.

SPI was assembled in the same way as SPH, but there was no hot melt adhesive between the heat-shrinkable tube and the sample, and there was no pinhole in the heat-shrinkable tube. UPI was assembled in the same way as SPI, but there were four square openings in the heat-shrinkable tube to allow the pressurized oil to flow in, and the extensometers could also be clamped on the sample directly through the openings. To prevent the crushed concrete from flowing into the pressurized oil, some dense fiber was also placed in the openings of the heat-shrinkable tube on UPI. All the samples were assembled as shown in Fig. 1(b).

This test was carried out on an XTR-01 computer-controlled triaxial testing machine. The triaxial cell of the machine had a self-balancing function. The confining pressure and the pressure of the pressurized liquid were all provided by the pressurized liquid, and the pressure of the pressurized liquid in the experiment was equal to the confining pressure. The size of the sample and the force diagram are shown in Fig. 1(a). A total of five confining pressure levels were used in this study, namely, 5, 10, 20,

40, and 70 MPa. In addition, the strain produced by the confining pressure is ignored in this paper, because of the deformation of the heat-shrinkable sleeve and the hot melt adhesive. The experimental procedure was as follows.

1) Calibration of the LVDTs and the extensometers with a standard micrometer caliper; the error per millimeter was less than 2%.

2) Assembly of the sample as shown in Fig. 1(b).

3) Insertion of the sample into the triaxial cell of the testing machine.

4) After closing the triaxial cell, filling of the triaxial cell with oil and increase of the confining pressure to the required value.

5) Application of the axial load to the sample at a displacement increasing rate of 5×10^{-6} m/s. If there was some residual stress, the loading stopped when the axial strain reached 10%. If the sample lost all its bearing capacity, the loading ceased immediately.

6) Removal of the sample and photography to show the failure patterns of the sample. Before photographing SPH, the hot melt adhesive on the sample was removed.

3 Results and discussion

3.1 Comparison of the failure patterns

Before the test, five unsealed samples were exposed in the pressurized oil (70 MPa) for 2 h. After being removed, the samples were cleaned and cut into several parts. It could be seen that the thickness of the oil layer in samples was less than 1 mm, while the interiors of the samples were still dry. Therefore, the samples were regarded as impermeable in this study.

As shown in Fig. 2, shear fracture dominated the failure mode of SPI when the confining pressure was between 10 and 40 MPa, while several short vertical fractures were distributed in the shear zone when the confining pressure was 5 MPa. Under confining pressure of 70 MPa, there was an irregular shear fracture and several vertical fractures in the sample, and the sample was easily crushed by hand after the experiment.

It can be seen from Fig. 2, that the vertical tensile fracture dominated the failure mode of UPI under each confining pressure. The failure patterns of UPI under triaxial compression were similar to the failure pattern of the intact sample under uniaxial compression (Fig. 3), but the number of the vertical fractures in UPI under triaxial compression was far less than that in the intact sample under uniaxial compression. Additionally, the crushed ends of the split parts (UPI) occurred at the same end under the confining pressure of 5 and 10 MPa, and the crushed ends of the split parts occurred at different ends under the confining pressure of 20, 40, and 70 MPa.

Figure 2 shows that all the samples of SPH suffered shear failure, but there were always vertical fractures originated from the cavity wall. It should also be noted, for all the visible vertical fractures originated from the cavity wall, that the vertical fractures did not originate from the roof or floor of the cavity, but from the sidewall of the cavity. As described in the previous Ref. [24] on rocks, these vertical tensile fractures originating from the sidewall can be referred to as the secondary tensile fractures. As shown in Fig. 2, the secondary tensile fractures originated from the sidewall of the cavity of various sizes under each confining pressure.

As shown in Fig. 2, there were also some vertical fractures generated from the shear fracture, but far away from the cavity, in several samples of SPH. These fractures must have originated during the propagation of the shear fractures, and this is great evidence that the shear fractures started from the sidewall failure because, for SPH, there was no residual stress in most of the samples. In other words, these vertical fractures generated from the shear fractures could not initiate after the shear fractures extended to the boundary of the sample. Moreover, if the pressurized liquid did not flow into these vertical fractures generated from the shear fractures but far away from the cavity, these fractures would be arrested by the influence of the confining pressure.

3.2 Comparison of the failure mechanisms

According to the failure modes of the sample and the results of the previous Refs. [13,23–28,39–41], the failure mechanisms of all types of the samples were analyzed as follows.

Figure 4 shows the schematic diagram of the failure mechanism of SPI under triaxial compression. The samples themselves had some defects, arising during the manufacturing process, such as pores or micro-cracks. According to the results of the previous Refs. [13,39–41], as the axial stress increases, the larger defects in the sample nucleate cracks firstly, and the cracks nucleated earlier grow along the direction of the maximum principal stress. However, the cracks nucleated earlier will stop extending because of the confinement of the confining pressure, and then the smaller defects nucleate new cracks as the axial stress continues increasing. When the shear stress ($\frac{\sigma_1 - \sigma_3}{2}$) reaches the ultimate shear stress of the sample, the defects in the shear band produce cracks spontaneously, leading to shear failure.

Figure 5 shows the schematic diagram of the failure mechanism of UPI under triaxial compression. The samples themselves had some defects that arose during the manufacturing process, and the pit on the surface could be in direct contact with the pressurized liquid. After the cracks nucleated from the pre-existing defects, the pressurized liquid could flow into them and weaken

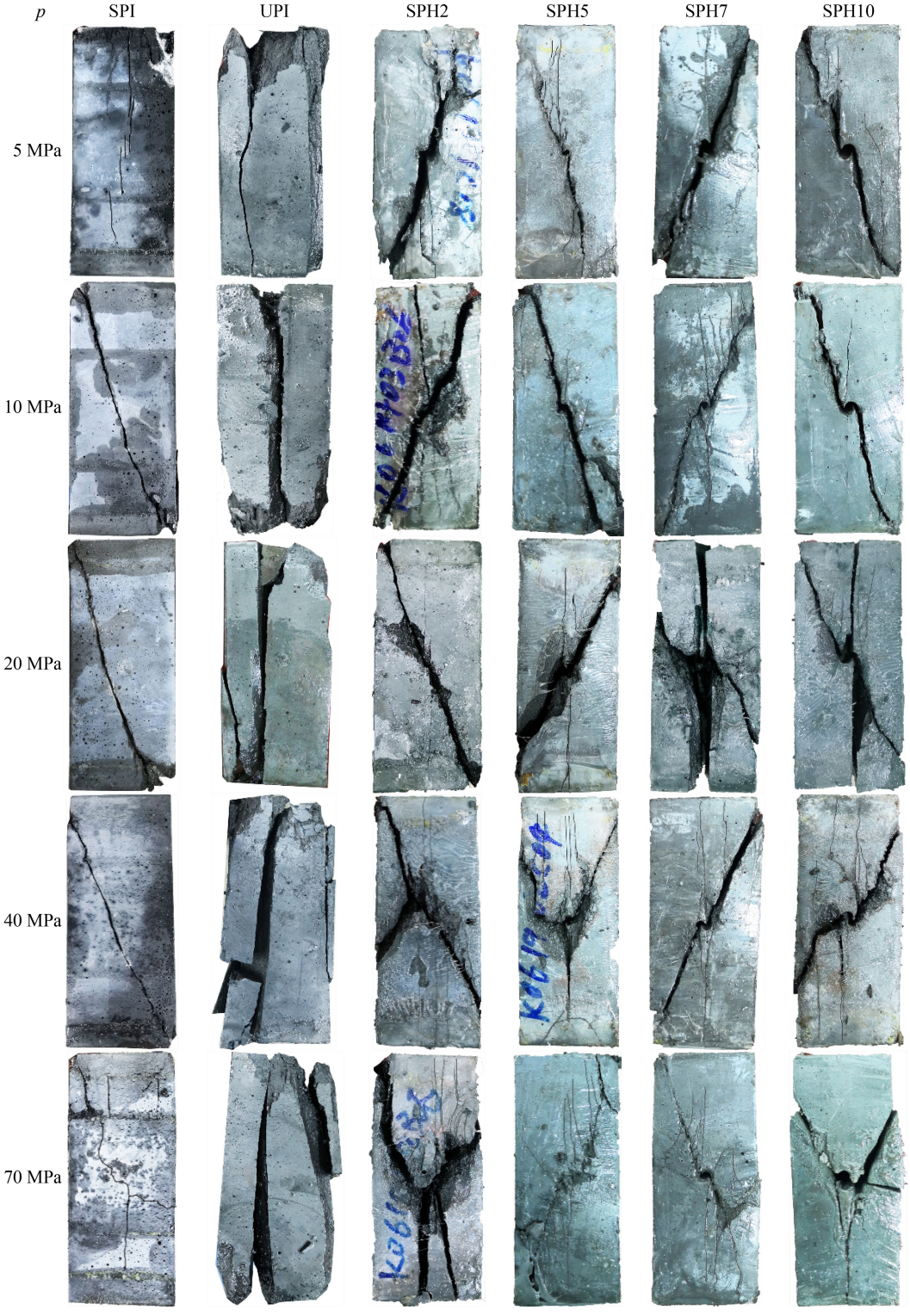

Fig. 2 Failure patterns of SPI, UPI and SPH.

the confinement effect of the confining pressure. The cracks without the confinement of the confining pressure became easier to propagate. As the axial stress continued to increase, one crack would extend to the end of the sample firstly. The sample was split into two parts. The increase in slenderness ratio, the deviation between the direction of the tensile fracture and the direction the axial load, or the distribution of the cracks nucleated from the pre-existing defects caused one end of the split sample to be crushed. It should be noted that under the confining pressures of 5 and 10 MPa, the crushed ends of the two split parts were in the same end of the sample, as shown

in Fig. 2. In this case, the sequence between the crushing of the end and the initiation of the tensile fracture could not be determined. Under the confining pressure of 20, 40, and 70 MPa, the crushed ends of the two split parts were in different ends of the sample. Therefore, it can be determined that the end crushing must have occurred after the initiation of the tensile fracture under the confining pressure of 20, 40, and 70 MPa.

Figure 6 shows the schematic diagram of the failure mechanism of SPH under triaxial compression. The sample has had a prefabricated cavity and some other pre-existing defects, and the pressurized liquid could only contact the surface of the cavity directly. As the axial stress increased, the stress concentration at the cavity caused sidewall failure. The sidewall failure took the form of the initiation of the first secondary tensile fracture, and the pressurized liquid could then flow into the secondary tensile fracture through the cavity. The effect of confinement of the confining pressure on the secondary tensile fracture was weakened. In addition, the pre-existing defects could also nucleate cracks. The origination sequence of the sidewall failure and the crack initiation from the pre-existing defects depended on the confining pressure and the cavity size. The fractures without pressurized liquid could be arrested by the confining pressure, and then the smaller defects could nucleate cracks. As the axial stress continued to increase, shear fractures propagated from the sidewall failure, and the secondary tensile fractures continued to extend. As the axial load continued to increase, the shear fractures continued to extend, and more vertical tensile fractures initiated from the shear fractures. If the pressurized liquid flowed through the entire shear fractures, the sample lost stability as soon as the shear fractures extended to the boundary of the sample. However, if the confining pressure was large enough, the shear fractures could be

Fig. 3 Failure pattern of the intact sample under uniaxial compression.

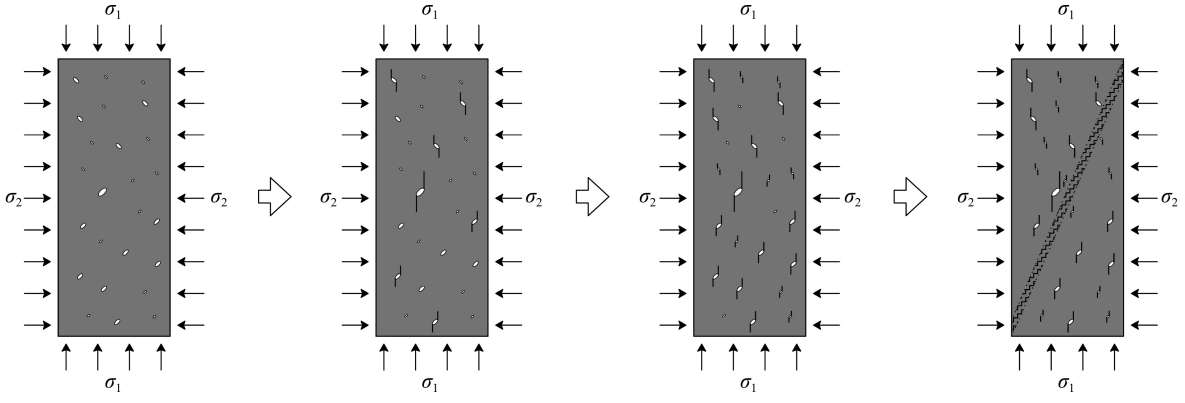

Fig. 4 Schematic diagram of the failure mechanism for SPI.

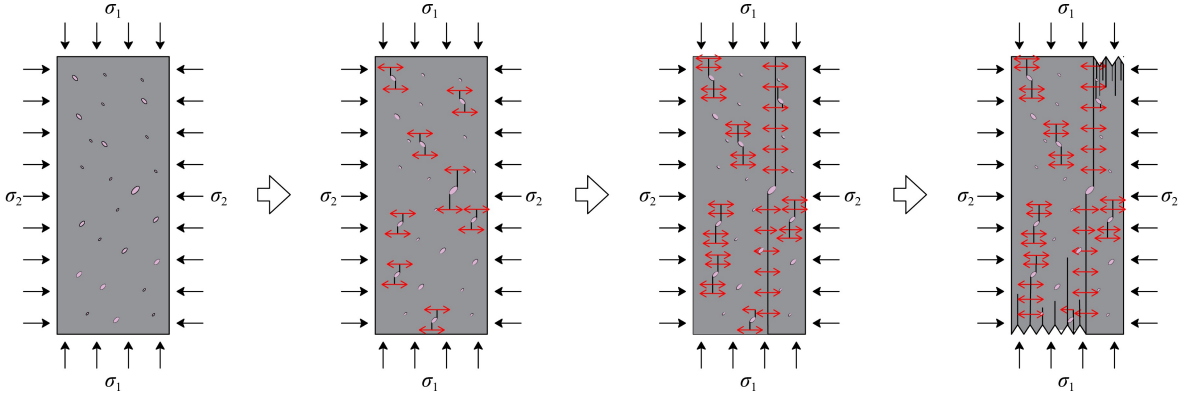

Fig. 5 Schematic diagram of the failure mechanism for UPI. Note: The red arrows indicate the pressure of the liquid.

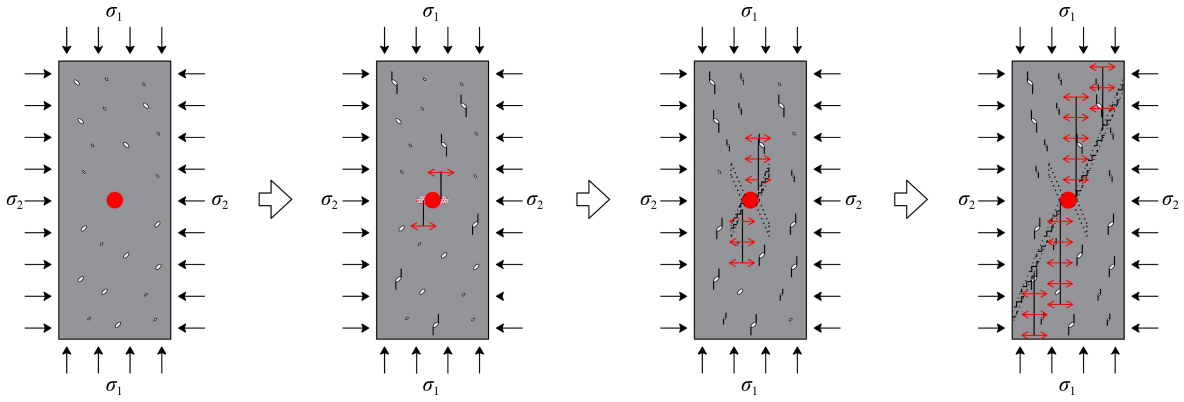

Fig. 6 Schematic diagram of the failure mechanism for SPH.

squeezed and closed, preventing the pressurized liquid from flowing into the entire shear fracture.

3.3 Relationship between the axial stress and the strains

Figure 7 demonstrates the axial deviatoric stress (q) and the lateral strain (ε_2) corresponding to the same axial strain (ε_1) under each confining pressure. It should be noted that, in order to make the graph tidier, not all the vertical coordinates of ε_2 are listed in Fig. 7. In fact, all the ε_2–ε_1 curves start at zero in the plots.

Under each confining pressure, there was always some residual stress in SPI as shown in Fig. 7, while there was always no residual stress in UPI as shown in Fig. 8. Additionally, there was no residual stress in all the samples of SPH when the confining pressure was between 5 and 20 MPa, while several samples of SPH had residual stress under the confining pressures of 40 and 70 MPa. For SPI, the confining pressure led the sample to remain stable after shear failure. For UPI, the crushing failure at the end of the sample occurred easily, resulting in no residual stress. For SPH, whether there was residual stress remaining depended on whether the pressurized liquid flowed through the entire shear fracture. If the pressurized liquid flowed through the entire shear fracture, the confining pressure could not confine the sample, and the sample easily lost stability, leading to no residual stress. If there was some residual stress in SPH, it could be indicated that the pressurized liquid did not flow through the entire shear fracture. It could be inferred, under the confining pressure of 40 and 70 MPa, that the shear fractures could be squeezed and closed, preventing the pressurized liquid from flowing through the entire shear fracture.

It should be noted that there is always an obvious knee point in each ε_2–ε_1 curve of SPH, while there is no obvious knee point in each ε_2–ε_1 curve of SPI. The knee points in the ε_2–ε_1 curves mean the beginning of the unstable propagation of the cracks, and the discontinuous segments in the ε_2–ε_1 curves mean the end of the shear failure. It can be seen that the axial stress of SPH reached its peak value after the knee point but before the discontinuous segment in the curves (Fig. 7). In other words, the axial stress of SPH reached its peak value during the process of the propagation of the shear fractures. Thus, it can be inferred that the fracture propagation reduced the bearing capacity of SPH.

As shown in Fig. 8, it was found, for UPI, that ε_2 increased almost linearly with the increase of ε_1 before the axial stress reached its peak value, and ε_2 increased sharply at peak stress. This indicates that the vertical tensile fracture propagation in UPI was an instantaneous process. However, according to the ε_2–ε_1 curves of SPH in Fig. 7, it can be seen that the increase of the lateral deformation in SPH was gradual. This was related to the propagation of the shear fractures in SPH. Moreover, it should be noted that the pressurized liquid could also flow into the secondary tensile fractures which originated from the cavity sidewall, but the propagation of the secondary tensile fractures in SPH was a gradual process, which was not like the propagation of the vertical tensile cracks in UPI. This is because the sample outside the shear fractures and the secondary tensile fractures in SPH was always confined by the confining pressure, while the vertical tensile cracks that could not be confined by the confining pressure were distributed throughout UPI.

3.4 The axial peak stresses and the corresponding axial strains

The triaxial compressive strengths of SPI, UPI, and SPH are given in Table 3, and the average axial peak stresses are plotted in Fig. 9(a). The axial strains at peak stress are plotted in Fig. 9(b). As shown in Fig. 9, it was found that both σ_1^{u} and $\varepsilon_1^{\mathrm{u}}$ of UPI were always between those of SPH2 and SPH10. This was mainly caused by the different failure mechanisms and different sealing conditions between UPI and SPH. The strength of UPI depended on the initiation of the fracture nucleated from the pre-existing defects of the sample, while the strength of SPH reached its peak value during the propagation of the shear fracture. According to the results shown in Fig. 8, the propagation of the vertical tensile fractures in UPI was an instantaneous process, and UPI lost its

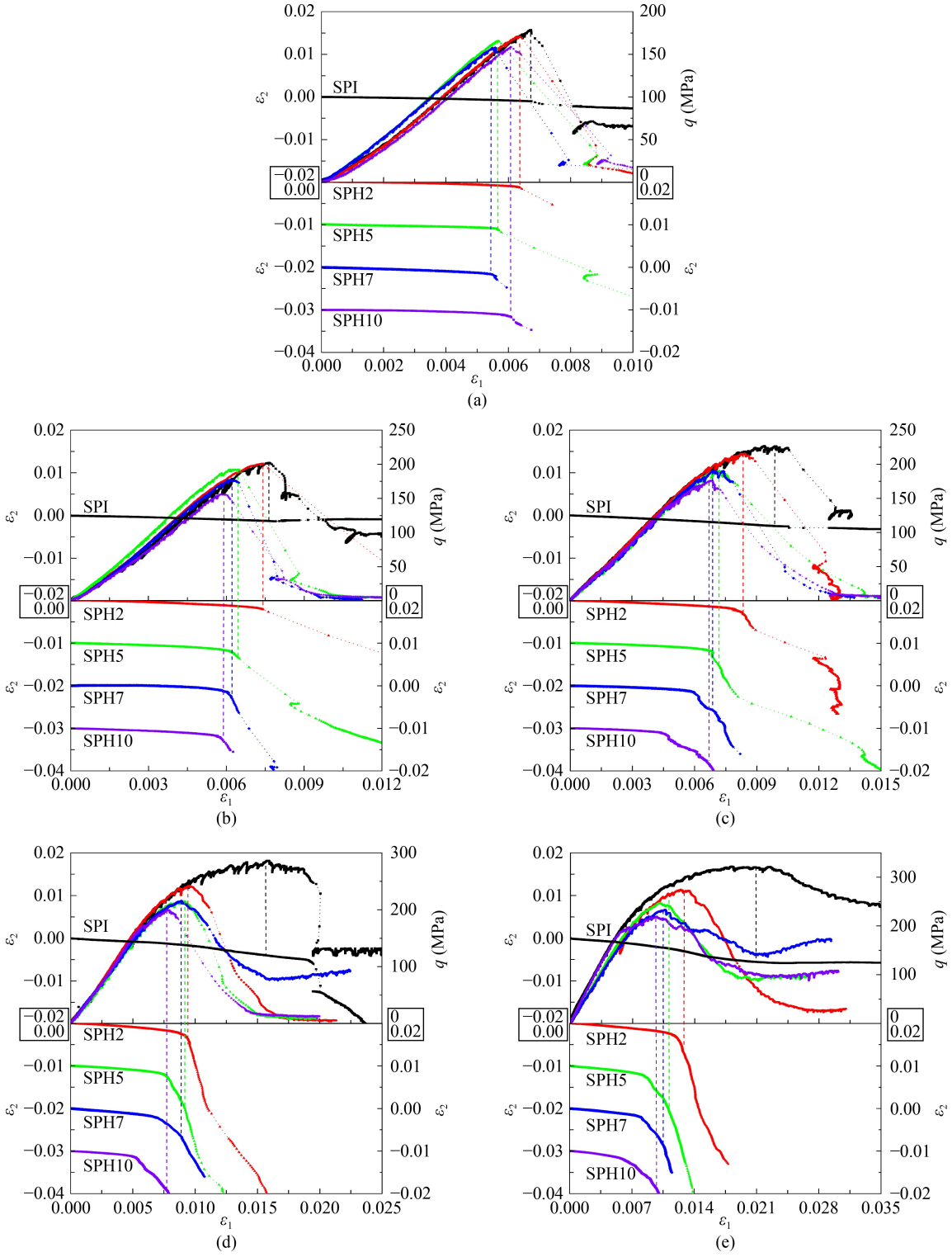

Fig. 7 q–ε_1 curves and ε_2–ε_1 curves for SPI and SPH. (a) p = 5 MPa; (b) p = 10 MPa; (c) p = 20 MPa; (d) p = 40 MPa; (e) p = 70 MPa.
Note: Curves of the same color refer to the same sample and the vertical dashed line corresponds to the peak stress.

bearing capacity completely once the vertical tensile fractures began propagating. Therefore, the axial peak stress of UPI can be regarded as the axial stress that can lead the fractures to be nucleated from the pre-existing defects. By comparing the strength of UPI and SPH, it can be inferred whether the pre-existing defects in SPH nucleate cracks. If the strength of SPH is larger than that of UPI, there must be cracks nucleated from the pre-existing defects of SPH before the axial stress reaches its peak value. If the strength of SPH is less than that of UPI, the pre-existing defects far away from the cavity cannot nucleate cracks, while the pre-existing defects around the

cavity may nucleate cracks because of the stress concentration.

Figure 9 shows that both σ_1^u and ε_1^u increased as the confining pressure increased for the same type of sample. In addition, the cavity size had an obvious effect on the strength and the axial deformation of the HPC samples. Focusing on the sample of SPI and SPH (SPI is one kind of SPH when the cavity size is zero), it was found that both σ_1^u and ε_1^u decreased as the cavity size increased

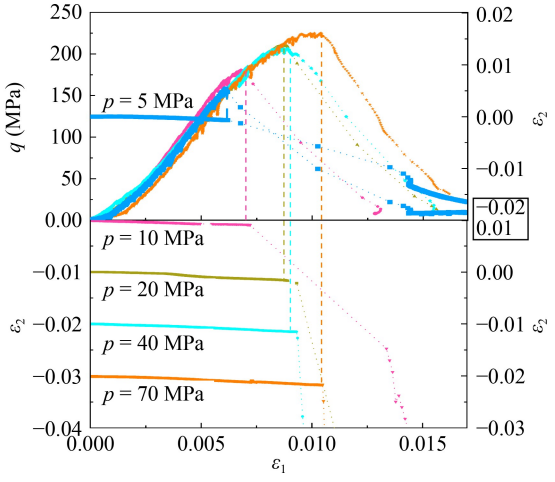

Fig. 8 q–ε_1 curves and ε_2–ε_1 curves of UPI. Note: Curves of the same color refer to the same sample and the vertical dashed lines correspond to the axial peak stress.

under each confining pressure. Therefore, the cavity weakened the triaxial compressive strength and the corresponding axial deformation.

Based on the above conclusions, it is necessary to give a failure criterion that can predict the triaxial compressive strength of HPC with a cavity. Richart et al. [42] proposed an empirical formula to predict the strength of ordinary concrete expressed as Eq. (1). This formula has played a great role in engineering application. In order to give a simple and effective formula for predicting strength in engineering application, cavity size can be added to the failure criterion as an influence factor.

According to Fig. 9, both the cavity size and the confining pressure had a great effect on the triaxial compressive strength of HPC. On the one hand, the cavity size and the confining pressure jointly determined the stress concentration of the cavity. On the other hand, the pressurized liquid in the shear fractures and the secondary tensile fractures weakened the confinement of the confining pressure and then weakened the triaxial strength of the sample. Therefore, in the failure criterion, the cavity size and the confining pressure need to be combined and added (Eq. (2)).

As an improved model, the Power-law failure criterion is more suitable for HPC [9,43–45], and it can be expressed as Eq. (3). In this study, the Power-law criterion can fit the triaxial compressive strength of SPI, as shown in Eq. (5). After the cavity size is added to

Table 3 The axial peak stress of SPI, UPI, and SPH

p (MPa)	axial peak stress (MPa)					
	SPI	UPI	SPH2	SPH5	SPH7	SPH10
0	140.1	140.1	–	–	–	–
0	146.3	146.3	–	–	–	–
0	139.8	139.8	–	–	–	–
5	177.3	163.3	175.847	179.3116	175.9208	156.8198
5	183.5	159.1	184.1258	181.9131	167.5052	162.3003
5	169.8	155.9	–	–	–	–
10	212.1	191	211.9001	208.3154	201.6341	186.669
10	216.2	189.2	223.3365	210.718	192.5688	193.1564
10	214.1	–	–	–	–	–
20	251.4	230.1	254.8578	236.8297	230.2449	210.3614
20	247	225.3	252.3076	245.208	238.378	210.3417
20	252.7	225.8	–	–	–	–
40	319.5	247.3	322.6123	292.1734	288.4725	265.5269
40	326.3	249.1	316.6082	292.0641	294.1774	264.7601
40	–	235.4	–	–	–	–
70	392	295.1	386.0612	361.7528	346.8041	329.3212
70	369.3	296.2	379.6329	350.6812	348.8799	327.4678
70	391.2	318.4	–	–	–	–

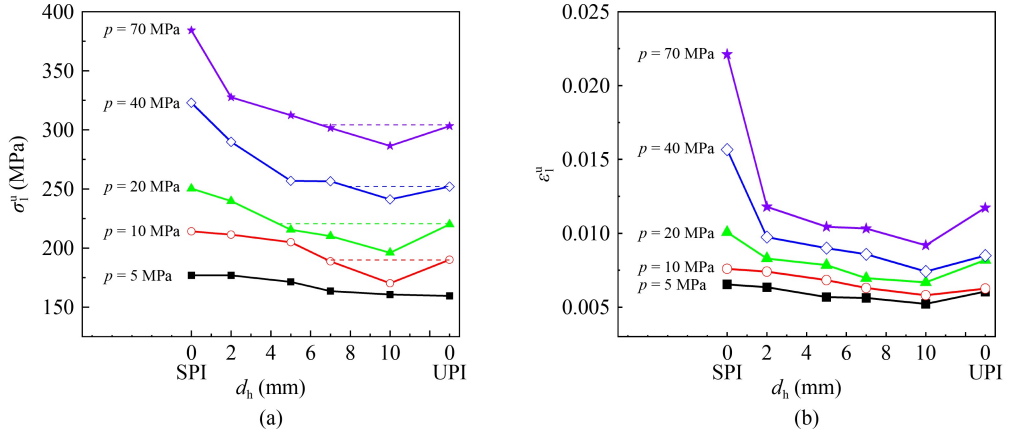

Fig. 9 The axial peak stresses and the corresponding axial strains. (a) σ_1^u–d_h; (b) ε_1^u–d_h. Note: The horizontal dashed lines correspond to the peak axial stress of UPI. σ_1^u is the axial peak stress; ε_1^u is the axial strain at peak stress.

Eq. (3) as an impact factor, it can be expressed as Eq. (6). In Eqs. (1)–(3) and (6), k_1, k_2, and a are empirical parameters, and f_c is the uniaxial compressive strength of HPC.

When the cavity size is zero, SPI can also be regarded as one kind of SPH. Therefore, σ_1^u of SPI and SPH are fitted into the same equation, while σ_1^u of UPI is excluded. Finally, Eq. (7) is obtained by fitting the triaxial compressive strength of SPI and SPH. According to the coefficient of determination, it can be deduced that Eq. (7) can well predict the effect of the cavity size and the confining pressure on the triaxial compressive strength of HPC.

$$\frac{\sigma_1}{f_c} = 1 + k_1 \frac{\sigma_3}{f_c}, \tag{1}$$

$$\frac{\sigma_1}{f_c} = 1 + k_1 \frac{\sigma_3}{f_c} + k_2 \frac{d_h \sigma_3}{l_2 f_c}, \tag{2}$$

$$\frac{\sigma_1}{f_c} = 1 + k_1 \left(\frac{\sigma_3}{f_c}\right)^a, \tag{3}$$

$$f_c = 142.1 \text{ MPa}, \tag{4}$$

$$\frac{\sigma_{1-\text{SPI}}^u}{f_c} = 1 + 2.74 \left(\frac{\sigma_3}{f_c}\right)^{0.66}, R^2 = 0.9912, \tag{5}$$

$$\frac{\sigma_1}{f_c} = 1 + k_1 \left(\frac{\sigma_3}{f_c}\right)^a + k_2 \frac{d_h \sigma_3}{l_2 f_c}, \tag{6}$$

$$\frac{\sigma_1^u}{f_c} = 1 + 2.74 \left(\frac{\sigma_3}{f_c}\right)^{0.66} - 12.90 \frac{d_h \sigma_3}{l_2 f_c}, R^2 = 0.9502. \tag{7}$$

Equation (7) cannot explain the effect of the propagation of the shear fractures and the secondary tensile fractures on the triaxial compressive strength of SPH, although it can well fit the triaxial compressive strength of SPH. Therefore, this experimental scheme needs to be further improved to get the effect of the propagation of the shear fractures and the secondary tensile fractures on the triaxial compressive strength.

3.5 The initiation and unstable propagation of the fractures in SPH

q–ε_1 curves, ε_v–ε_1 curves, ε_2–ε_1 curves, and ε_3–ε_1 curves of SPH and SPI are presented in the same graph (Fig. 10) under the same confining pressure, and the vertical dashed lines connect the peak point of the volumetric strain ($\varepsilon_v = \varepsilon_1 + \varepsilon_2 + \varepsilon_3$) and the corresponding deviatoric axial stress.

Referring to the failure patterns of SPH, the propagation of the shear fractures and the secondary tensile fractures advanced the increase of ε_2 but had no effect on the increase of ε_3. Therefore, the propagation of the shear fractures and the secondary tensile fractures caused the difference between ε_2 and ε_3 for the same sample. In addition, Fig. 10 shows that the ε_2–ε_1 curve and ε_3–ε_1 curve of the same sample of SPI also diverge under the confining pressure of 40 and 70 MPa, while the ε_2–ε_1 curve and ε_3–ε_1 curve of the same sample of SPI almost overlap when the confining pressure is lower than 40 MPa. The difference between ε_2 and ε_3 of SPI is related to the difference between the two sides of the cross-section of the sample, and the surfaces of the shear fractures of SPI were always parallel to l_3. However, Fig. 10 shows that the axial strain corresponding to the bifurcation point when the ε_2–ε_1 curve and the ε_3–ε_1 curve of the same sample of SPI diverge is larger than those in SPH, and the difference between ε_2 and ε_3 of SPI is far less than that of SPH, even when the confining pressures are 40 and 70 MPa. Therefore, in SPH, the bifurcation points when the ε_2–ε_1 curve and the ε_3–ε_1 curve diverge can be regarded as the initiation of the sidewall fracture.

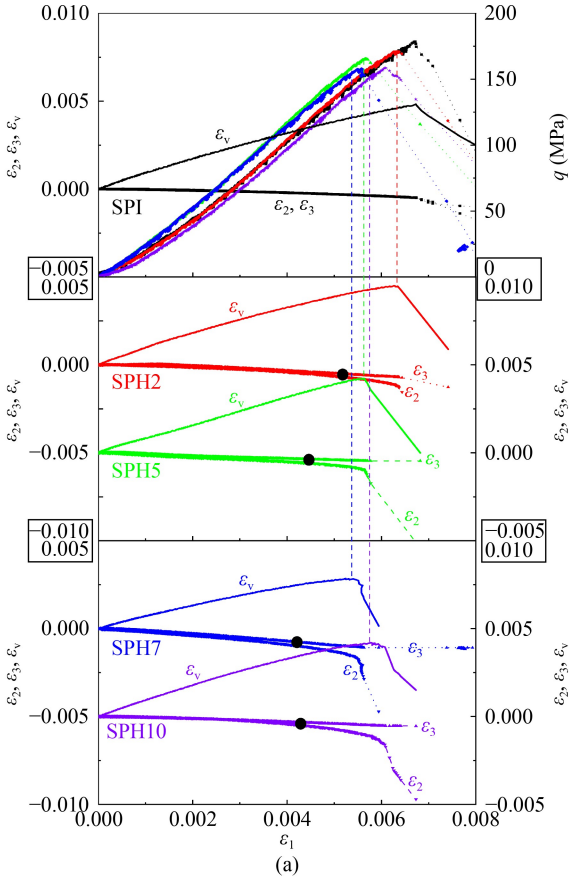
SPI
SPH2
SPH5
SPH7
SPH10
ε_v
$\varepsilon_2, \varepsilon_3$
ε_3
ε_2
q (MPa)
ε_1

(a)

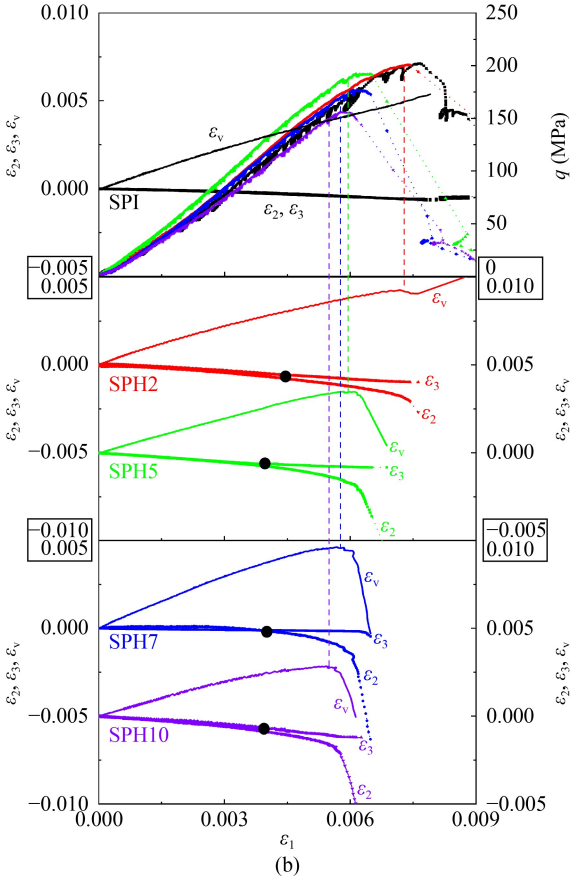
SPI
SPH2
SPH5
SPH7
SPH10
ε_v
$\varepsilon_2, \varepsilon_3$
ε_3
ε_2
q (MPa)
ε_1

(b)

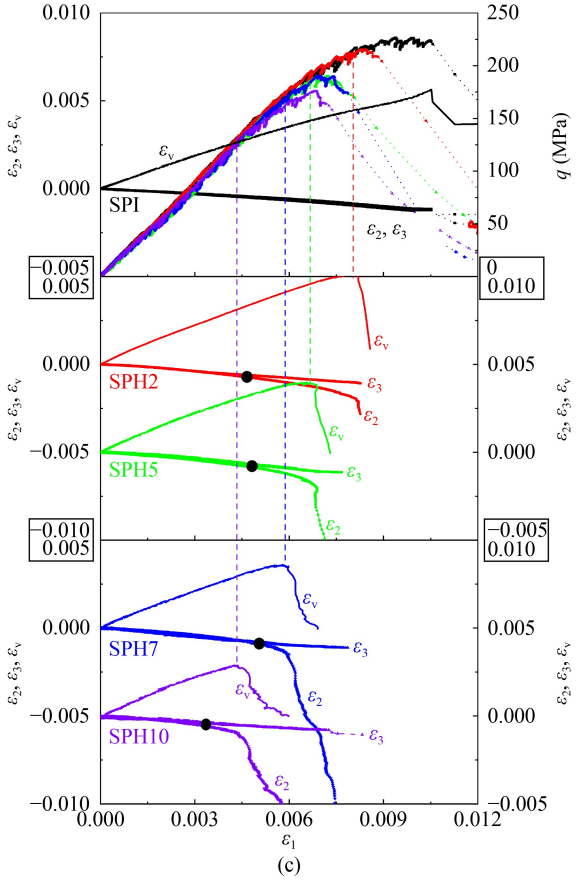
SPI
SPH2
SPH5
SPH7
SPH10
ε_v
$\varepsilon_2, \varepsilon_3$
ε_3
ε_2
q (MPa)
ε_1

(c)

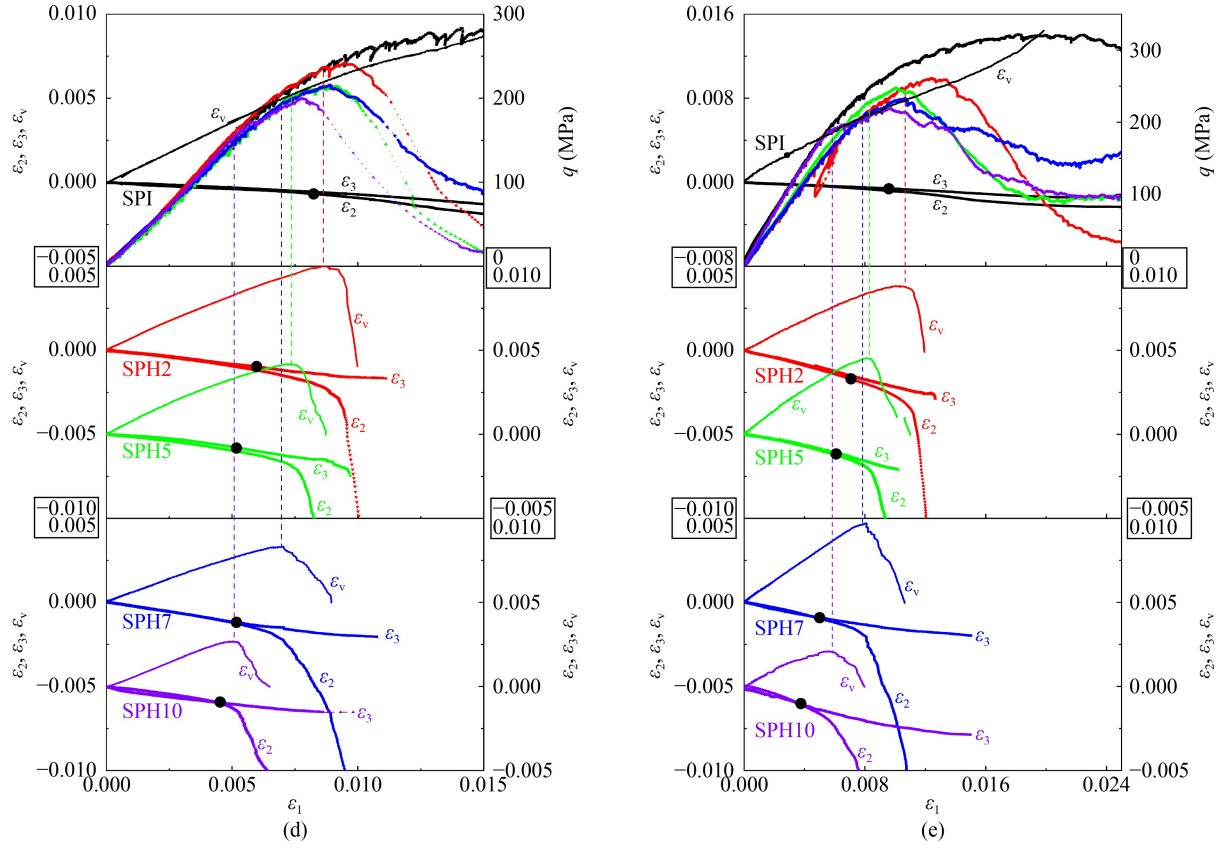

Fig. 10 q–ε_1 curves, ε_v–ε_1 curves, ε_2–ε_1 curves and ε_3–ε_1 curves of SPH and SPI. (a) p = 5 MPa; (b) p = 10 MPa; (c) p = 20 MPa; (d) p = 40 MPa; (e) p = 70 MPa. Note: Curves of the same color refer to the same sample; the vertical dashed lines correspond to the peak points of the ε_v–ε_1 curves; the points where the ε_2–ε_1 and ε_3–ε_1 curves diverge are marked with black dots; ε_v is the volumetric strain of the sample.

In order to better understand the effect of the cavity size and the confining pressure on the initiation of the sidewall fractures in SPH, the crack initiation stresses (σ_{ci}) are plotted in Fig. 11(a). It can be seen from Fig. 11(a) that the crack initiation stress (σ_{ci}) decreased as the cavity size increased under the confining pressure other than 20 MPa, and increased as the confining pressure increased. Therefore, to recap, the increase of the cavity size and the decrease of the confining pressure were all conducive to the sidewall failure.

It should be noted that the trend of the crack initiation stress with the aperture under the confining pressure of 20 MPa was different from the trend under other confining pressures. This may be caused by the inhomogeneity of the defects in the samples.

Additionally, according to the results in the previous literature [46–51], the peak value of the volumetric strain (ε_v^u) refers to the beginning of the unstable propagation of the fractures, and the corresponding axial peak stress is the crack damage threshold (σ_{cd}). Therefore, it can be considered that ε_v^u of SPH corresponds to the beginning of the unstable propagation of the fractures (the shear fractures and the secondary tensile fractures), and the corresponding σ_{cd} can be obtained. As shown in Fig. 10, ε_v of SPI increased with the increase of ε_1 before the axial stress reached its peak value, while ε_v of SPH always reached its peak value before the axial stress reached the peak value. Thus, it can be inferred that the pressurized liquid in the fractures advances the unstable propagation of the fractures. Additionally, both the cavity size and the confining pressure had a great effect on σ_{cd}, and further analysis of the effect of the cavity size and the confining pressure on σ_{cd} is plotted in Fig. 11(b).

It can be seen from Fig. 11(b) that σ_{cd} of the fractures in SPH decreased as the cavity size increased under each confining pressure, and increased as the confining pressure increased, except for one value of SPH10. Therefore, it is concluded that both the increase of the cavity size and the decrease of the confining pressure are conducive to the fracture propagation in SPH.

4 Conclusions

In order to research the influence of the cavity on the triaxial mechanical properties of HPC surrounded by pressurized liquid, this study explored a new experimental scheme. In this experiment, the samples (SPH) with a cavity of different sizes, the sealed (SPI) and unsealed (UPI) intact samples without a cavity were tested under conventional triaxial compression. For SPH, the pressurized liquid could only be in direct contact the

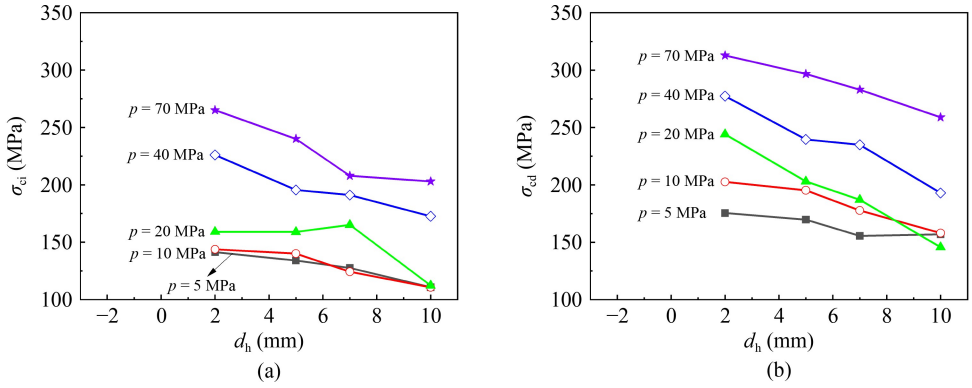

Fig. 11 The crack initiation stress and the crack damage threshold. (a) σ_{ci}–d_h; (b) σ_{cd}–d_h.

surface of the sample in the cavity, while the other surfaces were sealed. All surfaces of SPI were sealed, while all surfaces of UPI could be in direct contact the pressurized liquid.

Different cavity sizes can lead to different stress concentrations under different confining pressures, and the pressure of the liquid flowing into the fracture can weaken the confinement of the confining pressure. Therefore, under different confining pressures, HPC samples with a cavity of different sizes vary in terms of the strengths, failure modes, and deformation characteristics. The following conclusions can be drawn.

1) Under triaxial compression, the shear fracture dominates the failure mechanism of SPI, and the vertical tensile fracture dominates the failure mechanism of UPI. In addition, the shear fracture dominates the failure mechanism of SPH, while the secondary tensile fractures always originate from the cavity sidewall. Combined with the failure modes and the stress-strain curves, it can be inferred that the shear fractures initiate from the sidewall failure.

2) UPI loses its bearing capacity completely once the tensile fractures begin propagating, while the ultimate shear stress determines the triaxial compression strength of SPI. However, the axial stress of SPH reaches its peak value during the propagation of the shear fractures.

3) Under the confining pressure of 40 and 70 MPa, some residual stresses can be retained in several samples of SPH, while there is always no residual stress under lower confining pressures. This indicates that, if the confining pressure is large enough, the pressurized liquid cannot flow through the entire shear fractures.

4) Under each confining pressure, the triaxial compressive strength of SPH is negatively correlated with the cavity size. This paper gives a modified Power-law criterion to predict the strength of the sample, and the cavity size is added in this criterion as an impact factor.

5) The crack initiation stress and the crack damage threshold of the sidewall fractures in SPH can be obtained with this experimental scheme, and the experimental results show that both the decrease of the confining pressure and the increase of the cavity size are conducive to the initiation and unstable propagation of the fractures.

Acknowledgements The authors gratefully acknowledge the financial support by the National Natural Science Foundation of China (Grant Nos. 51279003 and 51078024).

References

1. Kassim M M, Ahmad S A. Strength evaluation of concrete columns with cross-sectional holes. Practice Periodical on Structural Design and Construction, 2018, 23(4): 04018027
2. Tahir M F, Shabbir F, Ahmad A, Ejaz N. Experimental and numerical investigation of transverse circular holes on load-carrying capacity of RC columns. Civil Engineering (Shiraz), 2021, 45(2): 683−696
3. Lotfy M E. Nonlinear analysis of reinforced concrete columns with holes. International Journal of Civil and Structural Engineering, 2013, 3(3): 655−668
4. Haeri H, Khaloo A, Marji M F. Fracture analyses of different pre-holed concrete specimens under compression. Chinese Journal of Theoretical and Applied Mechanics, 2015, 31(6): 855−870
5. Son K S, Pilakoutas K, Neocleous K. Behaviour of concrete columns with drilled holes. Magazine of Concrete Research, 2006, 58(7): 411−419
6. Fantilli A, Mihashi H, Vallini P, Chiaia B. The ductile behavior of high-performance concrete in compression. Archives of Civil Engineering, 2010, 56(1): 3−18
7. Williams E M, Graham S S, Akers S A, Reed P A, Rushing T S. Constitutive property behavior of an ultra-high-performance concrete with and without steel fibers. Computers and Concrete, 2010, 7(2): 191−202
8. Vankirk G, Heard W, Frank A, Hammons M, Roth J. Residual structural capacity of a high-performance concrete. Dynamic Behavior of Materials, 2019, 1: 233−236
9. Sovják R, Vogel F, Beckmann B. Triaxial compressive strength of ultra-high-performance concrete. Acta Polytechnica, 2013, 53(6): 901−905
10. Noori A, Shekarchi M, Moradian M, Moosavi M. Behavior of steel fiber-reinforced cementitious mortar and high-performance concrete in triaxial loading. ACI Materials Journal, 2015, 112(1): 95−103

11. Yu Z R, Qin X, An M Z. Experimental research on the conventional triaxial compressive properties of reactive powder concrete. China Railway Science, 2012, 33(2): 38−42 (in Chinese)
12. Wu L C, Wang Z, Liu D, Zhu H H, Lu Y, Lin L. Effect of Confining pressure and steel fiber volume content on mechanical property of reactive powder concrete. Journal of Building Materials, 2018, 21(2): 208−215 (in Chinese)
13. Zhang Y B, Wang Z. Effect of pressurized oil on the mechanical properties of reactive powder concrete. Journal of Advanced Concrete Technology, 2020, 18(12): 743−752
14. Ren J, Ge X. Computerized tomography examination of damage tests on rocks under triaxial compression. Rock Mechanics and Rock Engineering, 2004, 37(1): 83−93
15. Haimson B, Song I. Laboratory study of borehole breakouts in Cordova Cream: A case of shear failure mechanism. International Journal of Rock Mechanics and Mining Sciences & Geomechanics Abstracts, 1993, 30(7): 1047−1056
16. Lee M, Haimson B. Laboratory study of borehole breakouts in Lac du Bonnet granite: A case of extensile failure mechanism. International Journal of Rock Mechanics and Mining Sciences & Geomechanics Abstracts, 1993, 30(7): 1039−1045
17. Cheon D S, Jeon S, Park C, Ryu C. An experimental study on the brittle failure under true triaxial conditions. Tunnelling and Underground Space Technology, 2006, 21(3−4): 448−449
18. Cheon D S, Jeon S, Park C, Song W K, Park E S. Characterization of brittle failure using physical model experiments under polyaxial stress conditions. International Journal of Rock Mechanics and Mining Sciences, 2011, 48(1): 152−160
19. Haimson B. Micromechanisms of borehole instability leading to breakouts in rocks. International Journal of Rock Mechanics and Mining Sciences, 2007, 44(2): 157−173
20. Li T B, Wang X F, Meng L B. A physical simulation test for the rockburst in tunnels. Journal of Mountain Science, 2011, 8(2): 278−285
21. He M C, Xia H M, Jia X N, Gong W L, Zhao F, Liang K Y. Studies on classification, criteria and control of rockbursts. Journal of Rock Mechanics and Geotechnical Engineering, 2012, 4(2): 97−114
22. Kusui A, Villaescusa E, Funatsu T. Mechanical behaviour of scaled-down unsupported tunnel walls in hard rock under high stress. Tunnelling and Underground Space Technology, 2016, 60: 30−40
23. Hoek E. Rock Fracture under Static Stress Conditions. CSIR Report MEG 383. 1965
24. Wu H, Zhao G Y, Liang W Z. Investigation of cracking behavior and mechanism of sandstone specimens with a hole under compression. International Journal of Mechanical Sciences, 2019, 163: 105084
25. Einstein H H, Baecher G B, Hirschfeld R C. The effect of size on the strength of brittle rock. International Society of Rock Mechanics, 1970: 7−13
26. Carter B J, Lajtai E Z, Petukhov A. Primary and remote fracture around underground cavities. International Journal for Numerical and Analytical Methods in Geomechanics, 1991, 15(1): 21−40
27. Carter B J. Size and stress gradients effects on fracture around cavities. Rock Mechanics and Rock Engineering, 1992, 25(3): 167−186
28. Nesetova V, Lajtai E Z. Fracture from compressive stress concentrations around elastic flaws. International Journal of Rock Mechanics and Mining Sciences & Geomechanics Abstracts, 1973, 10(4): 265−284
29. Zhou S W, Zhuang X Y, Zhu H H, Rabczuk T. Phase field modelling of crack propagation, branching and coalescence in rocks. Theoretical and Applied Fracture Mechanics, 2018, 96: 174−192
30. Zhou S W, Zhuang X Y, Rabczuk T. Phase field modeling of brittle compressive-shear fractures in rock-like materials: A new driving force and a hybrid formulation. Computer Methods in Applied Mechanics and Engineering, 2019, 355(1): 729−752
31. Zhou S W, Rabczuk T, Zhuang X Y. Phase field modeling of quasi-static and dynamic crack propagation: COMSOL implementation and case studies. Advances in Engineering Software, 2018, 122: 31−49
32. Richard P, Cheyrezy M. Composition of reactive powder concretes. Cement and Concrete Research, 1995, 25(7): 1501−1511
33. Aïtcin P C. Science and Technology of Concrete Admixtures. Cambridge: Woodhead Publishing, 2016: 503−523
34. Scrivener K L, Bentur A, Pratt P. Quantitative characterization of the transition zone in high strength concretes. Advances in Cement Research, 1988, 1(4): 230−237
35. Scrivener K L, Crumbie A K, Laugesen P. The interfacial transition zone (ITZ) between cement paste and aggregate in concrete. Interface Science, 2004, 12(4): 411−421
36. Tam C M, Tam V W Y, Ng K M. Assessing drying shrinkage and water permeability of reactive powder concrete produced in Hong Kong. Construction & Building Materials, 2012, 26(1): 79−89
37. Roux N, Andrade C, Sanjuan M A. Experimental study of durability of reactive powder concrete. Journal of Materials in Civil Engineering, 1996, 8(1): 1−6
38. Li Z, Huang L D. Research on durability of reactive powder concrete with steel-fiber. Municipal Engineering Technology, 2005, 23(4): 255−257 (in Chinese)
39. Nemat-Nasser S, Horii H. Compression-induced nonplanar crack extension with application to splitting, exfoliation, and rockburst. Journal of Geophysical Research. Solid Earth, 1982, 87(B8): 6805−6821
40. Horii H, Nemat-Nasser S. Compression-induced microcrack growth in brittle solids: Axial splitting and shear failure. Journal of Geophysical Research, 1985, 90(B4): 3105−3125
41. Horii H, Nemat-Nasser S. Brittle failure in compression: Splitting, faulting and brittle-ductile transition. Philosophical Transactions of the Royal Society of London. Series A, Mathematical and Physical Sciences, 1986, 319(1549): 337−374
42. Richart F E, Brandtzaeg A, Brown R L. A study of the failure of concrete under combined compressive stresses. In: Bulletin No. 185, Urbana, IL: University of Illinois, 1928
43. Noori A, Shekarchi M, Moradian M, Moosavi M. Behavior of steel fiber-reinforced cementitious mortar and high-performance concrete in triaxial loading. ACI Materials Journal, 2015, 112(1): 95−103
44. Ren G M, Wu H, Fang Q, Liu J Z, Gong Z M. Triaxial

compressive behavior of UHPCC and applications in the projectile impact analyses. Construction & Building Materials, 2016, 113: 1−14

45. Wang H L, Li Q B. Prediction of elastic modulus and Poisson's ratio for unsaturated concrete. International Journal of Solids and Structures, 2007, 44(5): 1370−1379
46. Martin C D, Chandler N A. The progressive fracture of Lac du Bonnet granite. International Journal of Rock Mechanics and Mining Sciences & Geomechanics Abstracts, 1994, 31(6): 643−659
47. Zhao J, Feng X T, Zhang X W, Zhang Y, Zhou Y Y, Yang C X. Brittle-ductile transition and failure mechanism of Jinping marble under true triaxial compression. Engineering Geology, 2018, 232: 160−170
48. Li D Y, Sun Z, Xie T, Li X B, Ranjith P G. Energy evolution characteristics of hard rock during triaxial failure with different loading and unloading path. Engineering Geology, 2017, 228: 270−281
49. Huang Y H, Yang S Q, Tian W L. Crack coalescence behavior of sandstone specimen containing two pre-existing flaws under different confining pressures. Theoretical and Applied Fracture Mechanics, 2019, 99: 118−130
50. Zhang G B, Zhang W Q, Wang H L, Jia C, Liu K, Yu X, Song X. Microscopic failure mechanism analysis of sandstone under triaxial compression. Geotechnical and Geological Engineering, 2019, 37(2): 683−690
51. Yang S Q, Hu B, Tian W L. Effect of high temperature damage on triaxial mechanical failure behavior of sandstone specimens containing a single fissure. Engineering Fracture Mechanics, 2020, 233: 107066